

Electronic supplementary information (ESI)

Engineering of Lewis acid–base interfaces in Cu₂S/ZnIn₂S₄ hollow hetero-nanocages for enhanced photocatalytic CO₂ reduction

Yuanyuan Zhao^a, Kangjie Gao^b, Jiabin Li^a, Huanhuan Liu^{b,*}, Fang Chen^{c,*}, Wentao Wang^{c,*}, Yijun Zhong^a and Yong Hu^{b,*}

^aKey Laboratory of the Ministry of Education for Advanced Catalysis Materials, Department of Chemistry, Zhejiang Normal University, Jinhua 321004, China.

^bInstitute of Nanocatalysis and Energy Conversion, College of Chemistry and Materials Engineering, Zhejiang A&F University, Hangzhou 311300, China.

^cHangzhou Institute of Advanced Studies, Zhejiang Normal University, Hangzhou 311231, China.

^dGuizhou Provincial Key Laboratory of Computational Nano-Material Science, Guizhou Education University, Guiyang 550018, China.

* Corresponding authors.

E-mail addresses: yonghu@zafu.edu.cn (Y. Hu);

wtwang@gznc.edu.cn (W. Wang);

chenfang@zjnu.edu.cn (F. Chen);

hhuanliu@zafu.edu.cn (H. Liu).

Webpage: <https://www.x-mol.com/groups/yonghu>

1. Experimental section:

1.1 Materials

All the chemicals were analytical grade and purchased from Sinopharm Chemical Reagent Co., Ltd. (China) and directly used without further purification. Deionized (DI) water was used throughout the work.

1.2 Synthesis

CuS nanoboxes (NBs): Typically, an aqueous NaOH solution (20 mL, 1.25 M) was added into a mixture solution containing 0.375 g $\text{CuSO}_4 \cdot 5\text{H}_2\text{O}$, 0.147 g trisodium citrate and DI water (80 mL). After 15 min of stirring, L-ascorbic acid solution (50 mL, 0.03 M) was added to the suspension and stirred for 5 min before being left to stand for 1 h. Afterwards, the red precipitates of Cu_2O nanocubes (NCs) were isolated by centrifugation, followed by multiple washings with DI water and ethanol, and then dried at 60 °C overnight. Next, a Na_2S aqueous solution (40 mL, 6.25 mM) was introduced into a suspension of Cu_2O NCs (100 mg) in DI water (60 mL). After 30 min of stirring, the precipitate was collected by centrifugation and washed three times with DI water and ethanol, respectively. After dispersing the obtained $\text{Cu}_2\text{O}@ \text{CuS}$ core-shell NCs into a mixture of DI water (20 mL) and ethanol (20 mL), the alcoholic suspension was added by a $\text{Na}_2\text{S}_2\text{O}_3$ aqueous solution (16 mL, 1.0 M) for etching Cu_2O cores. After 30 min, CuS NBs were collected by centrifugation and washed three times with DI water and ethanol, respectively.

ZnIn₂S₄ nanosheets (NSs): ZnCl_2 (27.2 mg), TAA (60.1 mg) and $\text{InCl}_3 \cdot 4\text{H}_2\text{O}$ (117.2 mg) were dissolved into 8 mL of DI water and 2 mL glycerol. The solution was stirred for 15 min and then placed in the 80 °C water bath for 2 h. After cooling to ambient temperature, the product was collected by centrifugation, washed with ethanol, and dried at 60 °C for 12 h. Subsequently, the product was annealed in a

nitrogen atmosphere at 300 °C for 2 h with a heating rate of 2 °C min⁻¹.

Cu₂S/ZnIn₂S₄ HHNCs: Hierarchical Cu₂S/ZnIn₂S₄ HHNCs were prepared by hydrothermal and annealing steps. Specifically, a solution containing as-prepared CuS (8 mg), DI water (8 mL), and glycerol (2 mL) was sonicated for 30 min. Subsequently, ZnCl₂ (27.2 mg), TAA (60.1 mg) and InCl₃·4H₂O (117.2 mg) were added to the suspension under magnetic stirring for 15 min, followed by incubation in an 80 °C water bath for 2 h. The resulting CuS/ZnIn₂S₄ HHNCs were collected, washed with ethanol and dried at 60 °C overnight. Subsequently, the CuS/ZnIn₂S₄ HHNCs product was annealed in a nitrogen atmosphere at 300 °C for 2 h with a heating rate of 2 °C min⁻¹. The proportion of CuS and ZnIn₂S₄ in CuS/ZnIn₂S₄ HHNCs was adjusted by varying the amounts of precursor of ZnIn₂S₄. Detailedly, the amounts of ZnCl₂, InCl₃·4H₂O and TAA were 13.6 mg, 58.6 mg and 30 mg for CuS/ZnIn₂S₄-1 HHNCs; the amounts of ZnCl₂, InCl₃·4H₂O and TAA were 27.2 mg, 117.2 mg and 60.1 mg for CuS/ZnIn₂S₄-2 HHNCs; the amounts of ZnCl₂, InCl₃·4H₂O and TAA were 54.4 mg, 234.4 mg and 120 mg for CuS/ZnIn₂S₄-3 HHNCs, respectively. The mane of Cu₂S/ZnIn₂S₄-2 HHNCs is in line with Cu₂S/ZnIn₂S₄ HHNCs in this work.

Cu₂S/ZnIn₂S₄-mix: A physically mixed Cu₂S/ZnIn₂S₄-mix was prepared through a stirring method. Specifically, Cu₂S and ZnIn₂S₄ were dissolved in 20 ml of ethanol, and after being stirred for 6 h on the magnetic stirrer, the composite catalyst was obtained after drying in an oven.

1.3 Characterization

The phase constitution of samples was characterized by Powder X-ray diffractometer (XRD, Philips PW 3040/60, Cu K α radiation, scanning rate: 0.06 deg s⁻¹, Germany). Field-emission scanning electron microscopy (FESEM, GeminiSEM 300 scanning electron micro-analyzer) were applied to observe the morphological

characteristics of the samples. The accelerating voltage was 5 kV for FESEM observation. Transmission electron microscopy (TEM) and high-resolution TEM (HRTEM) images were acquired on a microscope (JEOL JEM-2100F, Japan) with a 200 kV accelerating voltage. X-ray photoelectron spectroscopy (XPS, ESCALab MKII X-ray photoelectron spectrometer, excitation source: Al K α X-ray, UK) was performed with an energy step size of 0.05 eV and passed energy of 20 eV to identify the surface element composition and chemical environments of elements in samples. In-situ irradiated XPS was conducted under a vacuum condition similar to common XPS tests, except that visible light was introduced into the test system. Ultraviolet photoemission spectroscopy (UPS) analysis was performed using the He I (21.22 eV) emission line for excitation, and the data was acquired with an energy step size of 0.02 eV and pass energy of 1.0 eV. Ultraviolet-visible diffuse reflectance spectra (UV-Vis DRS) were obtained by a Thermo Nicolet Evolution 500 UV-Vis spectrophotometer (Japan) to investigate the light-harvesting ability of samples. The specific surface area was evaluated by employing the Brunauer-Emmett-Teller (BET) method through nitrogen adsorption-desorption tests. In detail, the catalyst was first degassed at 150 °C for 4 h, and then measured at 77 K. CO₂ adsorption isotherms using a BSD-PS (M) apparatus (Beishide Instrument Technology (Beijing) Co., Ltd. China) was used to evaluate CO₂ adsorption ability of samples at 298 K. Prior to starting the measurement, the catalyst was first dried at 120 °C for 4 h to remove the water contained in the catalyst. The temperature-programmed desorption (TPD) of NH₃ and CO₂ was measured using a GC9790II equipped with a thermal conductivity detector (TCD). Raman spectra were collected on a LabRAM HR Evolution Raman spectrometer (UK) with an excitation light of 532 nm. The Fourier transform infrared (FTIR) spectra were collected using FTIR spectrometers (Nicolet NEXUS670, USA).

In-situ diffuse reflectance infrared Fourier transform spectra (In-situ DRIFTS) were collected on a Bruker INVENIO Fourier-transform infrared spectrometer (Karlsruhe, Germany), equipped with a mercury cadmium telluride (MCT) detector cooled by liquid nitrogen. Prior to adsorption, the samples were first purged with helium gas (30 mL min⁻¹) for 30 min at 120 °C. Then, a mixed gas flow consisting of 25 mL min⁻¹ of He, 5 mL min⁻¹ of CO₂, and a trace of H₂O vapor were introduced into the reactor. After reaching the adsorption equilibrium (~30 min), FTIR signals of samples with and without irradiation were collected with different irradiation time.

1.4 Photocatalytic CO₂ reduction tests

The PCR experiment was performed on a Labsolar-6A system (Beijing Perfectlight, China) with a MicroSolar 300 Xeon lamp (Beijing Perfectlight) and a 400 nm cut-on filter as the visible light. Before the PCR, the catalyst was dispersed in 100 mL of deionized water and subsequently irradiated for 1 h to eliminate any surface organic contaminants throughout the entire catalyst preparation process.¹ And then, 5 mg of catalyst was dispersed in 2 mL deionized water under ultrasonication for 20 min, the suspension was plastered onto a rounded fiberglass paper (4 cm in diameter) and naturally dried at ambient temperature. As depicted in **Fig. S1**, the fiberglass paper containing the sample was fixed to a tripod and positioned within a homo-thermal (25 °C) Pyrex reaction vessel. Subsequently, 2 mL of deionized water was added to the bottom of the reactor. The reaction vessel was vacuumed and the high-purity CO₂ (99.99%) was injected into the reaction systems to reach around 80 kPa. The reaction vessel was enclosed by aluminum foil to avoid light interference from the surroundings. The average light intensity (P) was 249.3 mW cm⁻² for the visible light resource with a 400 nm cut-on filter. The gas product was collected at an interval of 30 min and analyzed using an online gas chromatograph (Shimadzu Gas

Chromatograph GC-2014, Ar carrier, Japan) equipped with flame ionization detector (FID) and TCD. The isotope-labeling experiment was conducted under the identical reaction conditions, with the exception that $^{13}\text{CO}_2$ was utilized instead of $^{12}\text{CO}_2$. 0.5 mL of the gas product, along with a certain quantity of ethane as an internal standard substance (ISS), was collected by a gas-tight syringe and analyzed through gas chromatography-mass spectrometry (Agilent 7890B coupled to an Agilent 7000C inert XL MSD).

The product selectivity of CH_4 and CO was calculated using the following equations (1) and (2), respectively:

$$\text{Product selectivity (CH}_4\text{)} = \left(\frac{n(\text{CH}_4)}{n(\text{CH}_4) + n(\text{CO})} \right) \times 100\% \quad (1)$$

$$\text{Product selectivity (CO)} = \left(\frac{n(\text{CO})}{n(\text{CH}_4) + n(\text{CO})} \right) \times 100\% \quad (2)$$

where $n(\text{CH}_4)$ and $n(\text{CO})$ represent the yields (mol) of CH_4 and CO in a certain period, respectively.

1.5 Computational details

Density functional theory (DFT) based first-principles calculations were performed using the projected augmented wave (PAW)² method implemented in the Vienna *ab initio* simulation package (VASP).^{3,4} The Kohn-Sham one-electron states were expanded using the plane-wave basis set with a kinetic energy cutoff of 500 eV. The Perdew-Burke-Ernzerhof (PBE)⁵ exchange-correlation functional within the generalized gradient approximation (GGA) was employed. The ZnS-terminated (1×1) ZnIn_2S_4 (001) surface slab of seven layers is a rectangular cell of 7.850 Å by 7.850 Å, which can be nicely matched with 1×1 unit cell of Cu_2S (111) (7.853 Å by 7.853 Å). Thus, the Cu_2S (111)/ ZnIn_2S_4 (001) heterostructure were constructed. A $2 \times 3 \times 1$ supercell of Cu_2S (111)/ ZnIn_2S_4 (001) heterostructure was considered the starting

point of the theoretical calculation. For this heterostructure the x-axis, y-axis, and positions of all atoms were fully relaxed during the structure relaxation, while the z-axis was fixed to ensure the thickness of the vacuum slab. The optimized lattice constants of the Cu₂S (111)/ZnIn₂S₄ (001) lateral heterostructure were $u = 15.471 \text{ \AA}$ and $v = 24.856 \text{ \AA}$. The Brillouin-zone (BZ) integration was carried out using the Monkhorst-Pack⁶ sampling method with a density of $2 \times 1 \times 1$ for the geometry optimizations. A sufficiently large vacuum region of 20 \AA was used for all the systems to ensure the periodic images to be well separated. During the geometry optimizations, all the atoms were allowed to relax until the maximum magnitude of the force acting on the atoms smaller than 0.05 eV/\AA , and the total energy convergence criterion was set to $1 \times 10^{-4} \text{ eV}$. The atomic structures were analyzed by using the VESTA code⁷.

In the actual reaction, although the electrons come from the photogenerated electrons in the excited state of the material and the H⁺ originates from the cleavage of water molecules in solution, we still equated the free energy of the H⁺+ e⁻ pairs to half the free energy of an isolated H₂ molecule after using a computational hydrogen electrode⁸.

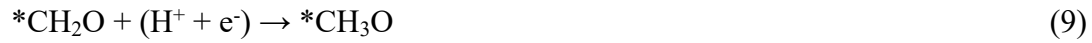
The free energy correction was obtained similarly by including the zero-point energy (ZPE) and entropic contributions from vibrational degrees of freedom calculated with the substrate fixed. The adsorption or reaction Gibbs free energy is defined as $\Delta G = \Delta E + (\text{ZPE} - T\Delta S)$, where ΔE is the adsorption or reaction energy based on DFT calculations. ΔZPE is the ZPE correction, T is the temperature (here T is 298.15 K), and ΔS is the entropy change. For each system, its ZPE can be calculated by summing vibrational frequencies overall normal modes ν ($\text{ZPE} = 1/2 \sum \hbar \nu$). The entropies of gas-phase H₂, CO, and CO₂ are obtained from the NIST

database⁹ with the standard condition, and the adsorbed species are only taken vibrational entropy (S_v) into account, as shown in the following formula:

$$S_v = \sum_i R \left\{ \frac{h\nu_i}{k_B T} \left[\exp\left(\frac{h\nu_i}{k_B T}\right) - 1 \right]^{-1} - \ln \left[1 - \exp\left(-\frac{h\nu_i}{k_B T}\right) \right] \right\} \quad (3)$$

Among which $R = 8.314 \text{ J}\cdot\text{mol}^{-1}\cdot\text{K}^{-1}$, $T = 298.15 \text{ K}$, $h = 6.63 \times 10^{-34} \text{ J}\cdot\text{s}$, $k_B = 1.38 \times 10^{-23} \text{ J}\cdot\text{K}^{-1}$, i is the frequency number, ν_i is the vibrational frequency (unit is cm^{-1}).

The free energy Diagram for electrochemical CO_2 reduction is made by considering the following steps:



2. Supplementary Figures:

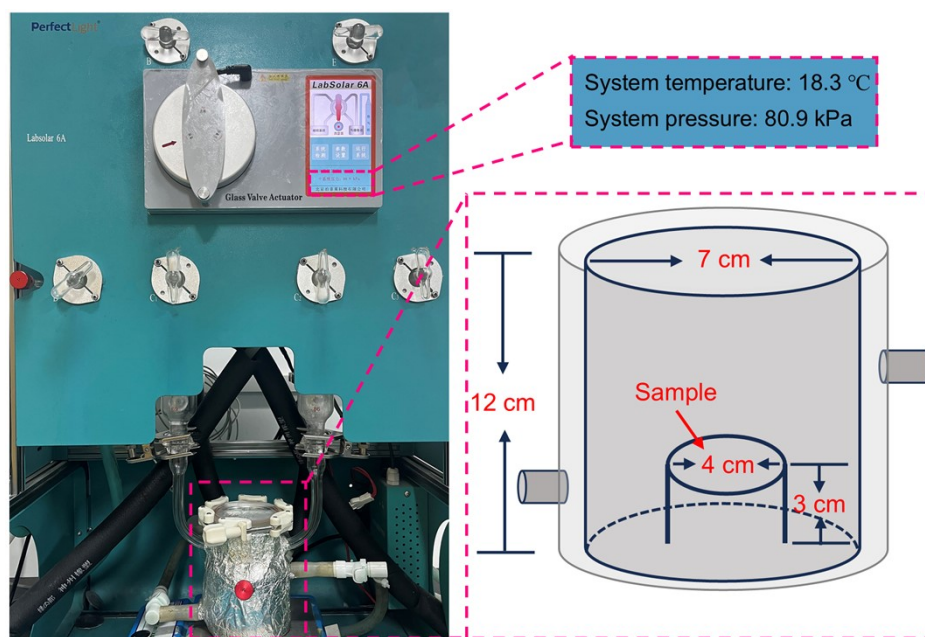


Fig. S1. The reaction equipment of the photocatalytic CO₂ reduction process.

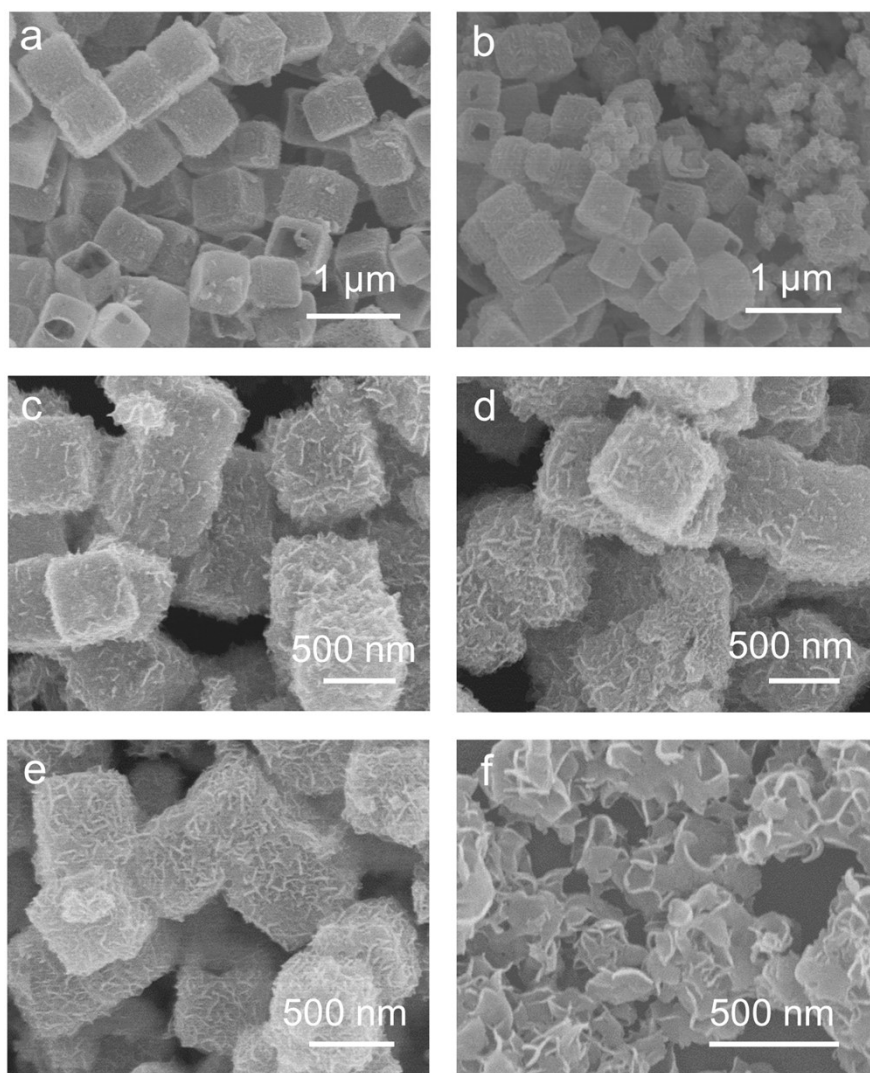


Fig. S2. FESEM images of the as-prepared (a) Cu₂S NBs, (b) Cu₂S/ZnIn₂S₄-mix, (c) Cu₂S/ZnIn₂S₄-1 HHNCs, (d) Cu₂S/ZnIn₂S₄-2 HHNCs, (e) Cu₂S/ZnIn₂S₄-3 HHNCs, (f) ZnIn₂S₄ NSs. The name of Cu₂S/ZnIn₂S₄-2 HHNCs is in line with Cu₂S/ZnIn₂S₄ HHNCs in this work.

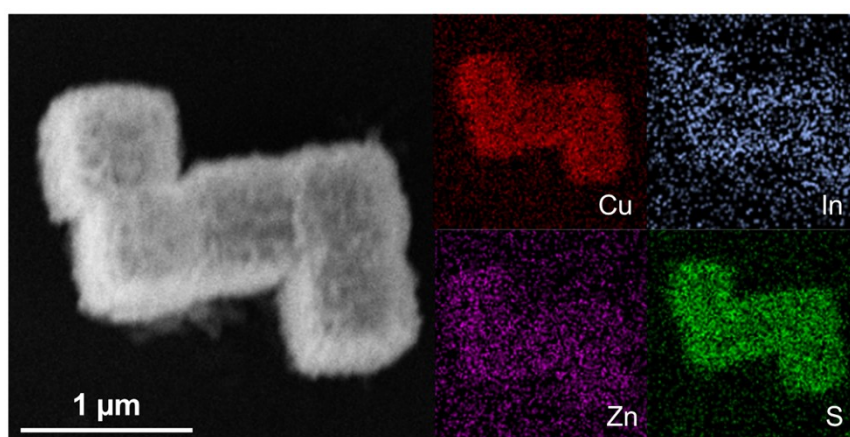


Fig. S3. STEM-EDS elemental mapping images of the as-prepared $\text{Cu}_2\text{S}/\text{ZnIn}_2\text{S}_4$ HHNCs.

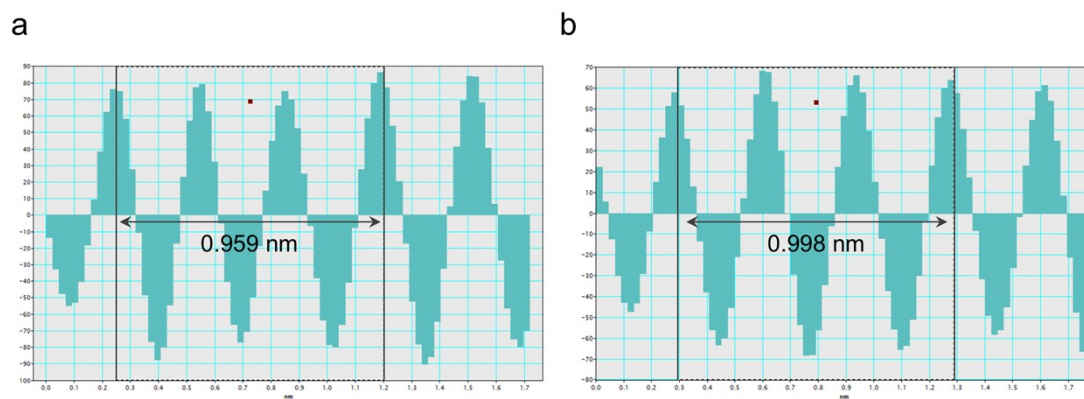


Fig. S4. Interplanar spacing of (a) Cu_2S and (b) ZnIn_2S_4 .

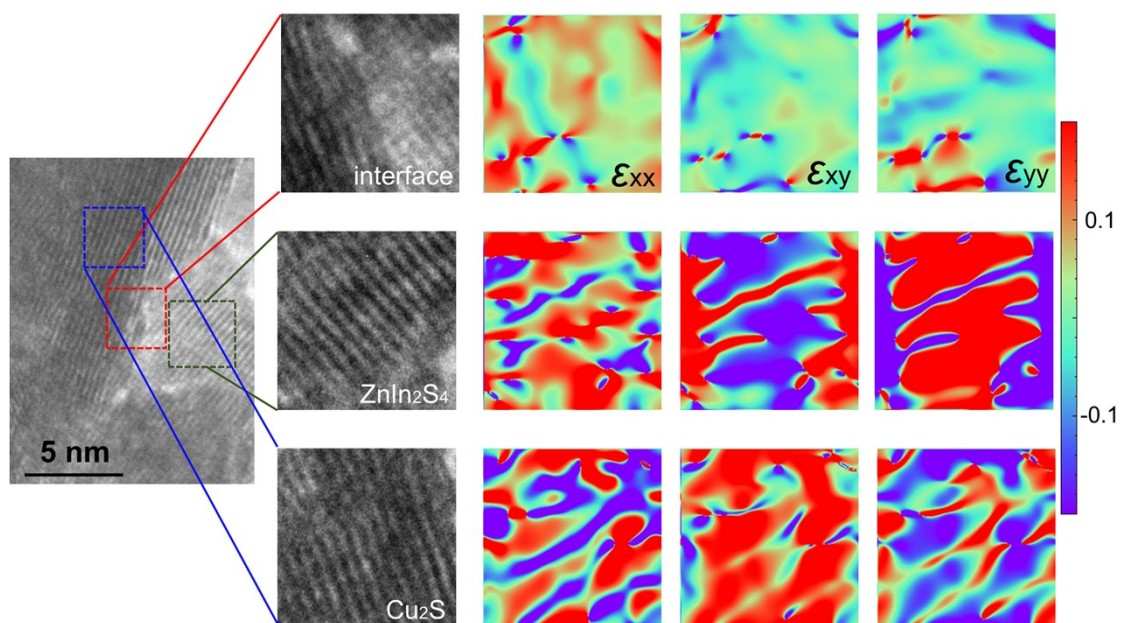


Fig. S5. HRTEM image strain component was determined via geometric phase analysis of the Cu₂S/ZnIn₂S₄ HHNCs.

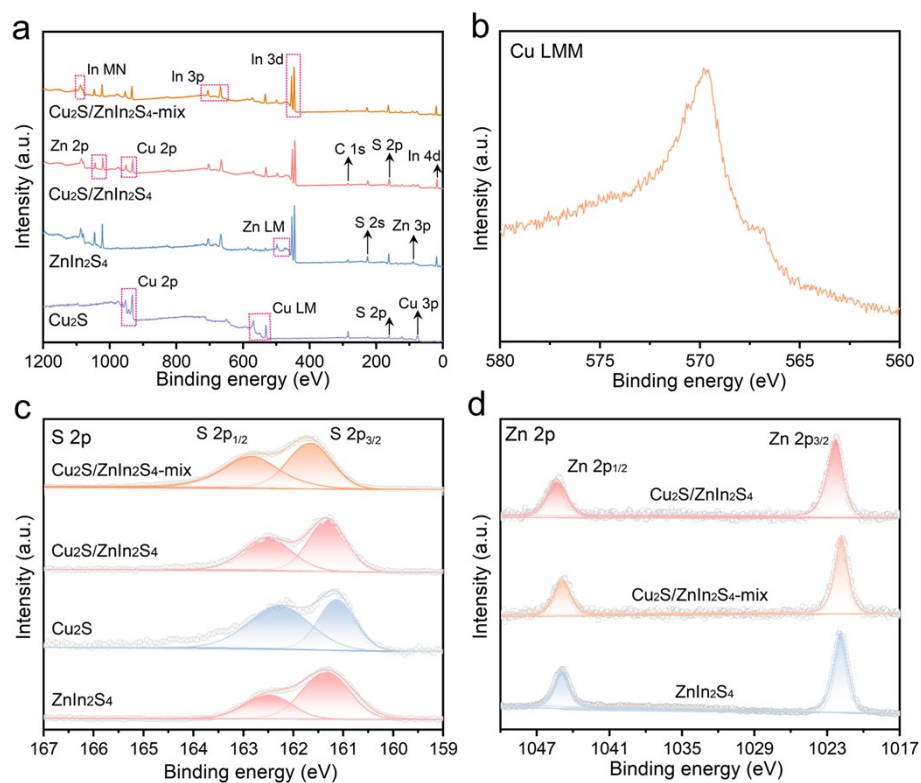


Fig. S6. (a) The survey spectra of the Cu₂S NBs, ZnIn₂S₄ NSs, Cu₂S/ZnIn₂S₄ HHNCs and Cu₂S/ZnIn₂S₄-mix. (b) The Auger Cu LMM XPS spectrum of the Cu₂S/ZnIn₂S₄ HHNCs. (c) S 2p and (d) Zn 2p high-resolution XPS spectra of the Cu₂S NBs, ZnIn₂S₄ NSs, Cu₂S/ZnIn₂S₄ HHNCs and Cu₂S/ZnIn₂S₄-mix.

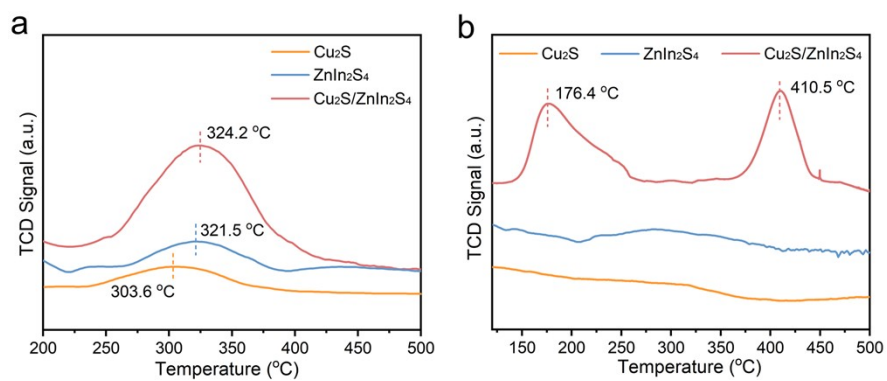


Fig. S7. (a) CO₂-TPD and (b) NH₃-TPD of the as-prepared Cu₂S NBS, ZnIn₂S₄ NSs, Cu₂S/ZnIn₂S₄ HHNCs.

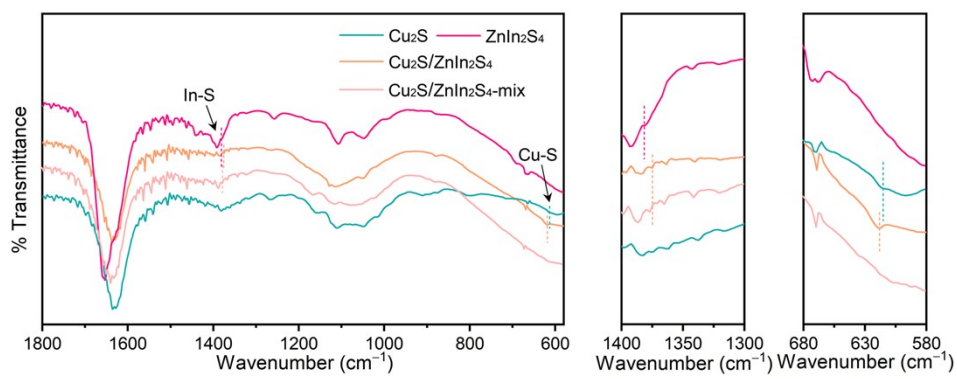


Fig. S8. FT-IR spectrum of the as-prepared Cu₂S NBs, ZnIn₂S₄ NSs, Cu₂S/ZnIn₂S₄ HHNCs and Cu₂S/ZnIn₂S₄-mix.

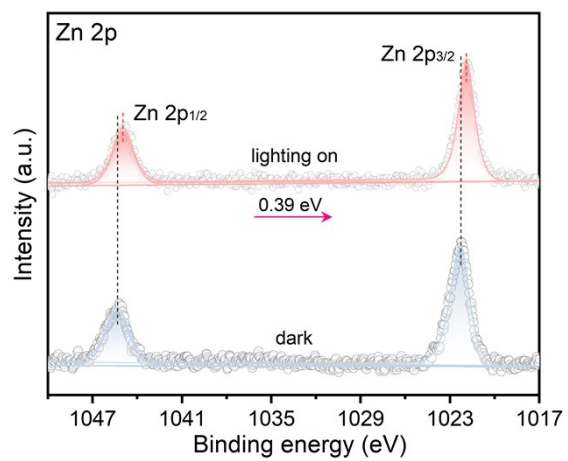


Fig. S9. Zn 2p high-resolution XPS spectra of Cu₂S/ZnIn₂S₄ HHNCs with and without irradiation.

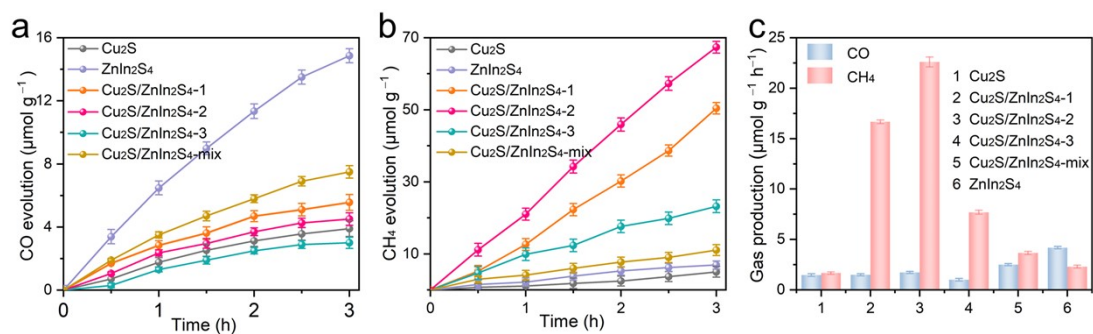


Fig. S10. Time courses of photocatalytic (a) CH₄ and (b) CO evolution on different catalysts under visible-light irradiation ($\lambda > 400$ nm) in gas-solid reaction system; error bars mean \pm standard deviations calculated from three independent measurements, (c) CH₄ and CO evolution rates over different samples. The man of Cu₂S/ZnIn₂S₄-2 HHNCs is in line with Cu₂S/ZnIn₂S₄ HHNCs in this work.

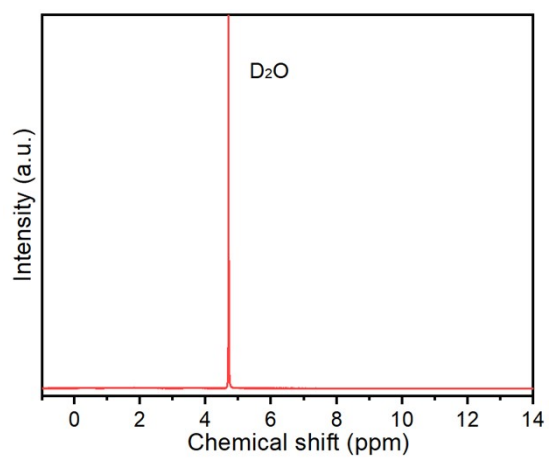


Fig. S11. ^1H -NMR spectra of the liquid phase taken from the reaction system of $\text{Cu}_2\text{S}/\text{ZnIn}_2\text{S}_4$ HHNCs after photocatalytic CO_2 reduction test.

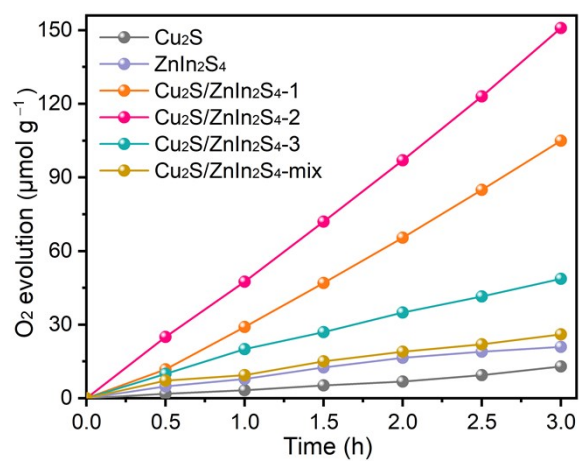


Fig. S12. Time courses of photocatalytic O₂ evolution on different catalysts under visible-light irradiation ($\lambda > 400$ nm) in gas-solid reaction system. The man of Cu₂S/ZnIn₂S₄-2 HHNCs is in line with Cu₂S/ZnIn₂S₄ HHNCs in this work.

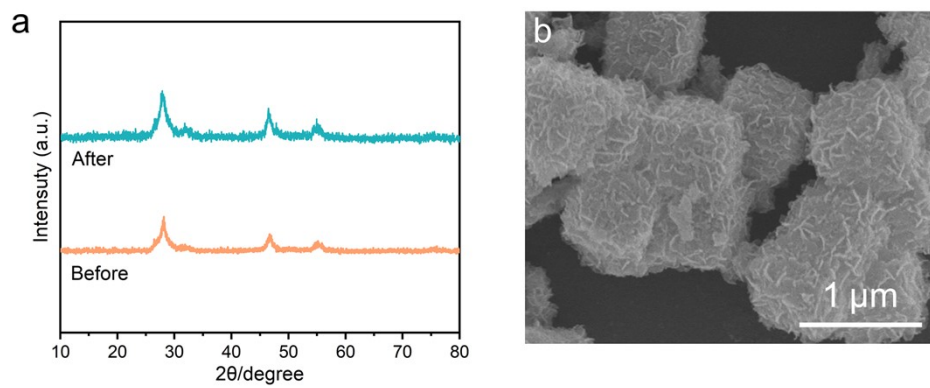


Fig. S13. (a) XRD patterns of the as-prepared $\text{Cu}_2\text{S}/\text{ZnIn}_2\text{S}_4$ HHNCs before and after cyclic tests, and (b) FESEM image of the as-prepared $\text{Cu}_2\text{S}/\text{ZnIn}_2\text{S}_4$ HHNCs after cyclic tests.

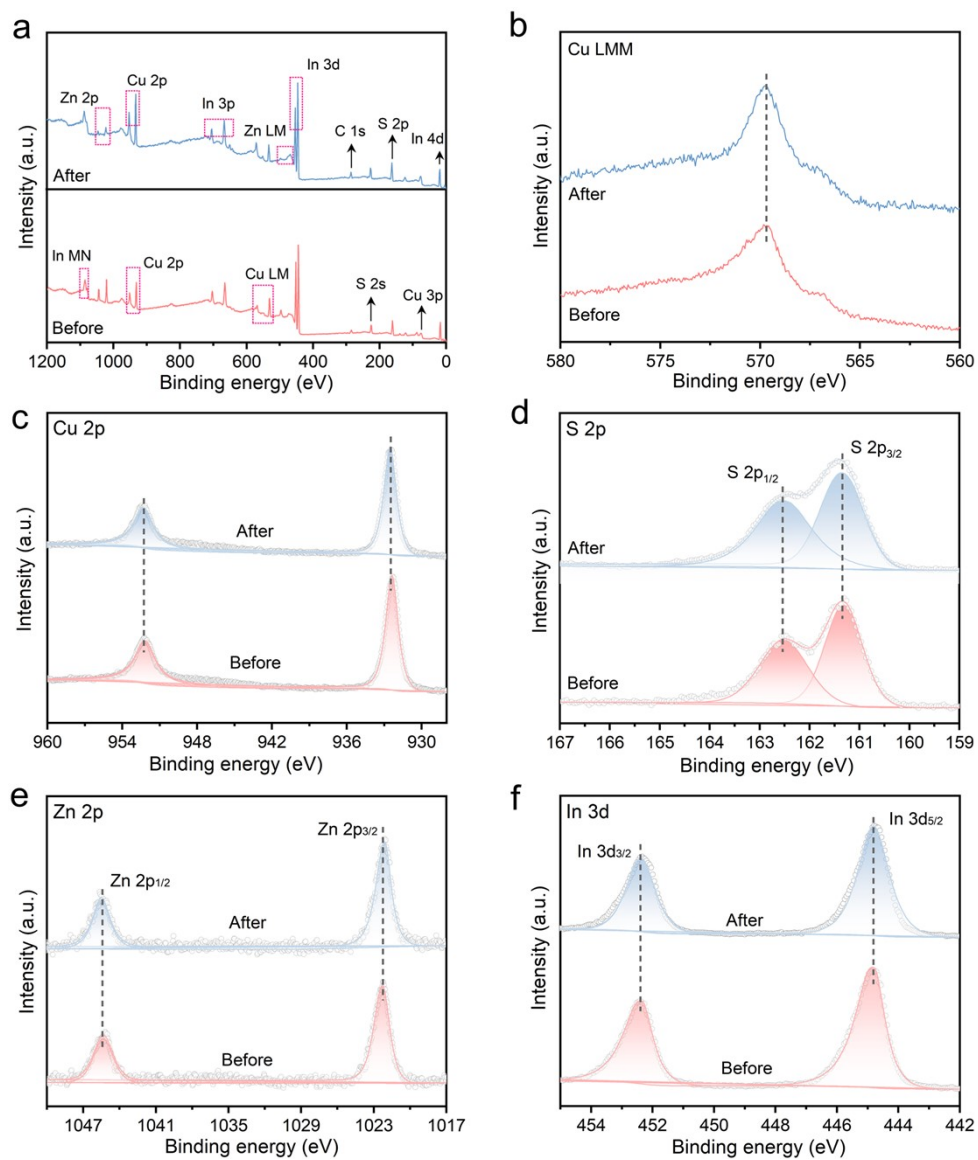


Fig. S14. (a) Survey, (b) Cu LMM, (c) Cu 2p, (d) S 2p, (e) Zn 2p, and (f) In 3d high-resolution XPS spectra of the as-prepared $\text{Cu}_2\text{S}/\text{ZnIn}_2\text{S}_4$ HHNCs before and after cyclic tests.

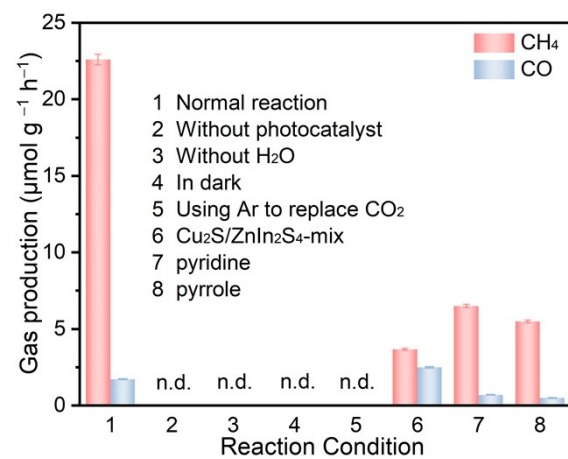


Fig. S15. CO₂ photoreduction activity under various reaction conditions.

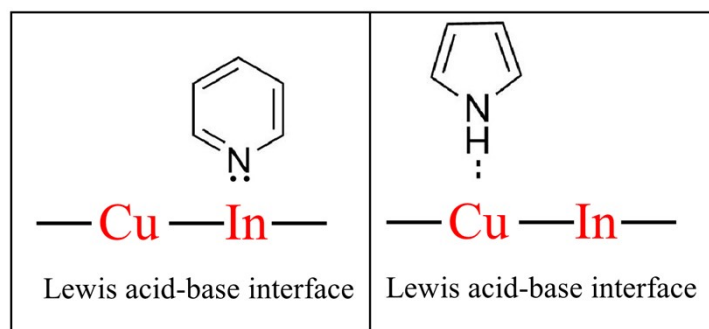


Fig. S16. Schematic diagram of adsorption of Lewis acid-base interface of different molecules.

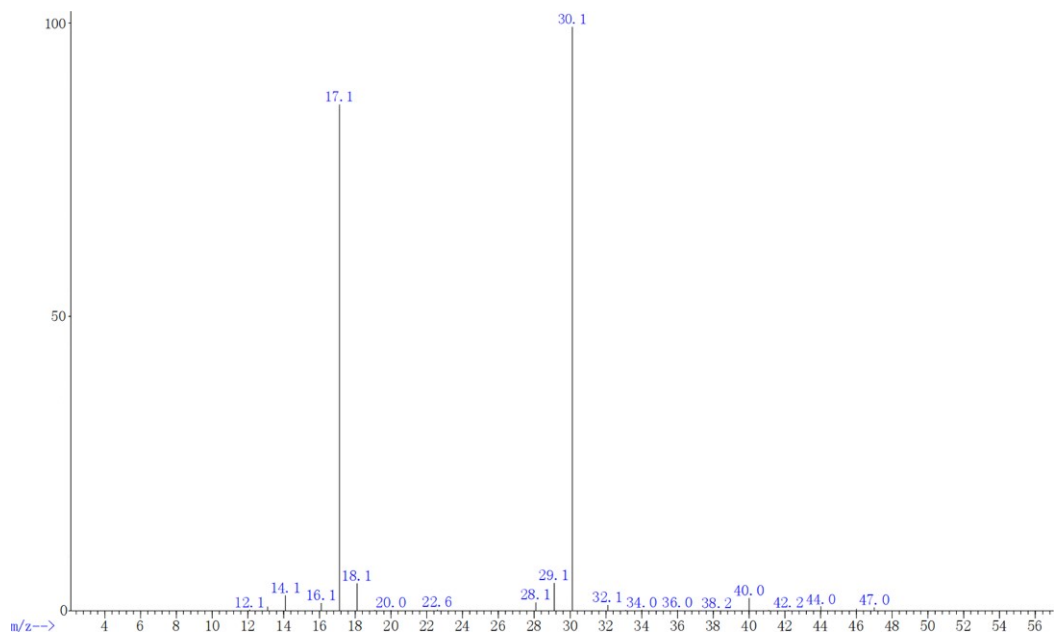


Fig. S17. Isotope-labeled mass spectra of gaseous products for photocatalytic reduction of $^{13}\text{CO}_2$ over $\text{Cu}_2\text{S}/\text{ZnIn}_2\text{S}_4$ HHNCs under visible-light irradiation for 1 h.

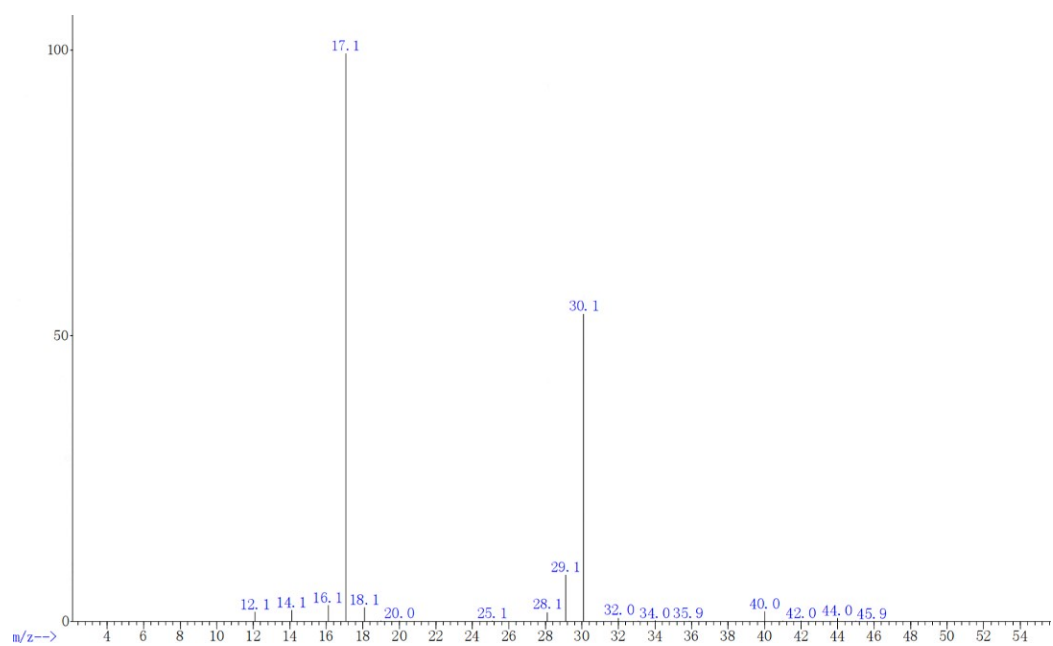


Fig. S18. Isotope-labeled mass spectra of gaseous products for photocatalytic reduction of $^{13}\text{CO}_2$ over $\text{Cu}_2\text{S}/\text{ZnIn}_2\text{S}_4$ HHNCs under visible-light irradiation for 2 h.

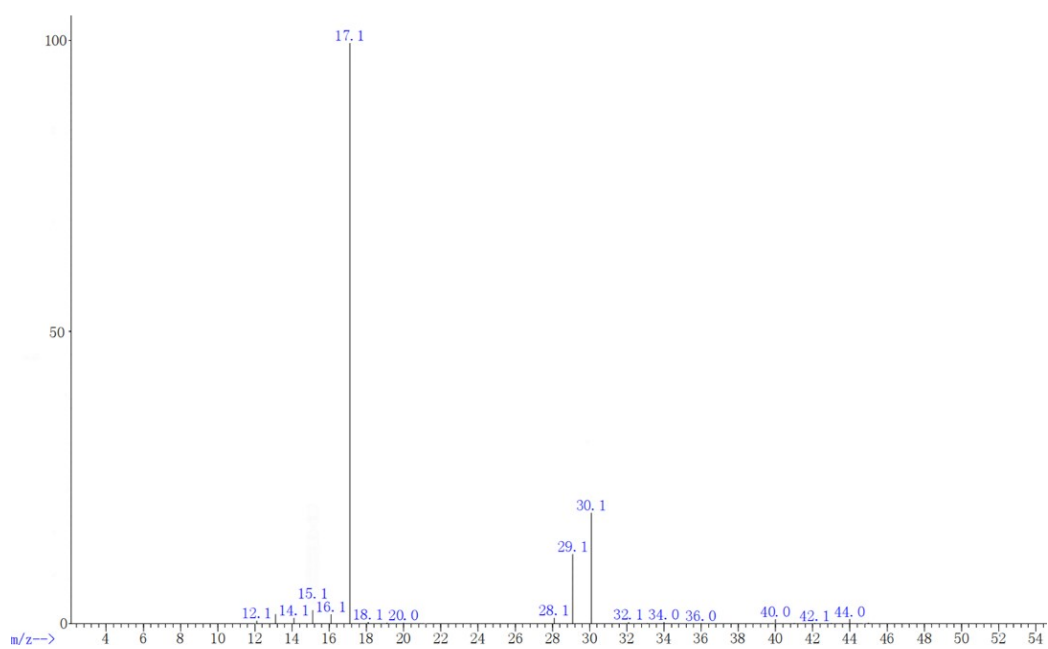


Fig. S19. Isotope-labeled mass spectra of gaseous products for photocatalytic reduction of $^{13}\text{CO}_2$ over $\text{Cu}_2\text{S}/\text{ZnIn}_2\text{S}_4$ HHNCs under visible-light irradiation for 3 h.

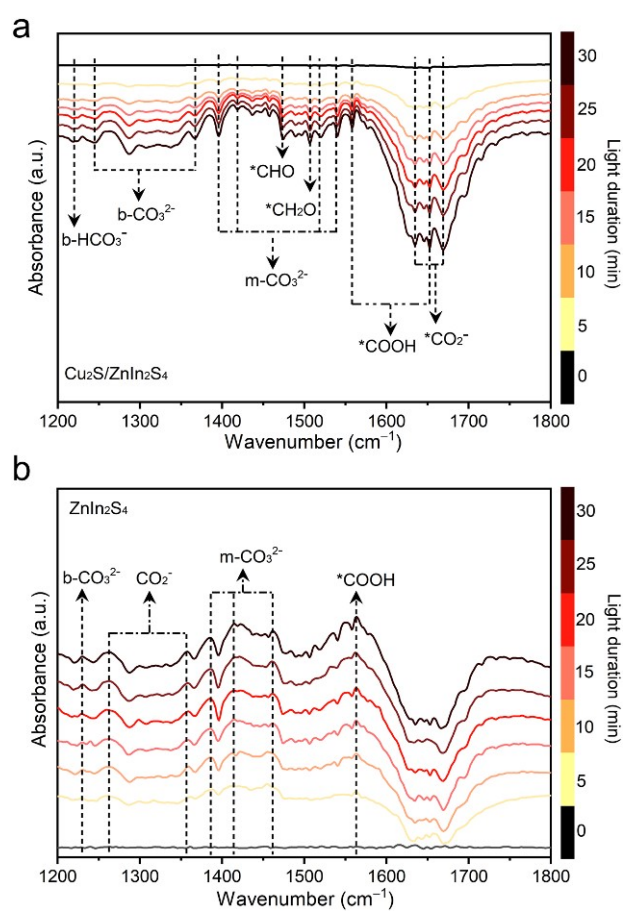


Fig. S20. In-situ DRIFTS of (a) the $\text{Cu}_2\text{S}/\text{ZnIn}_2\text{S}_4$ HHNCs and (b) ZnIn_2S_4 NSs exposed to a mixture gas of He, CO_2 , and H_2O with and without irradiation.

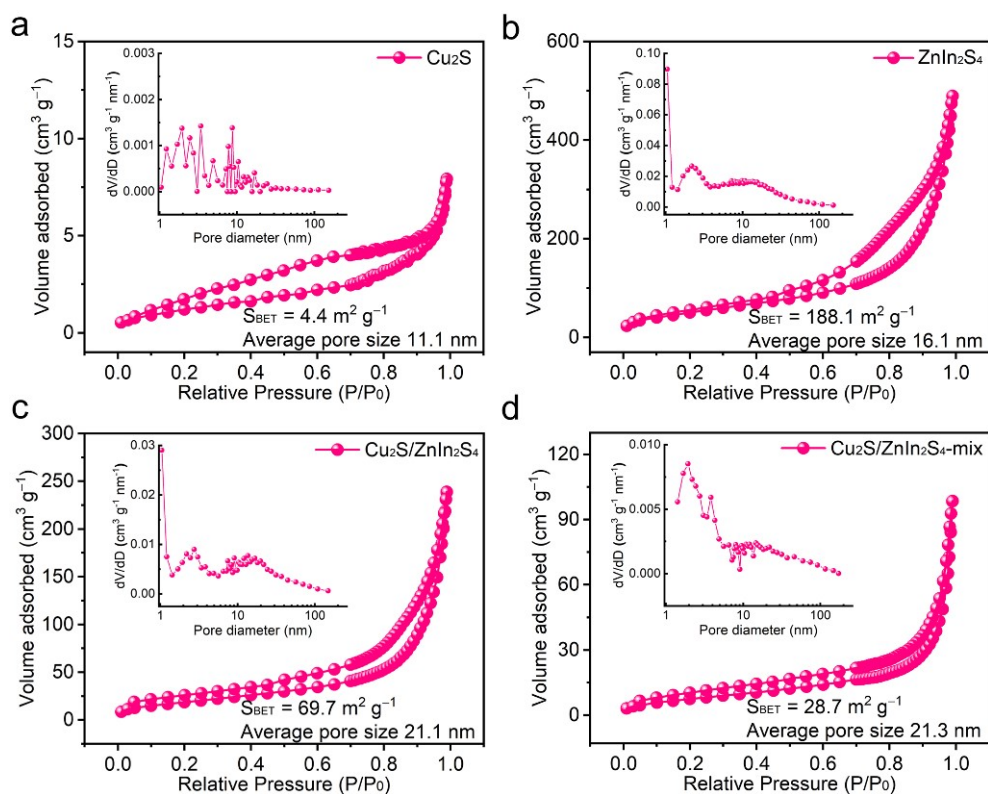


Fig. S21. Nitrogen adsorption-desorption isotherms of the as-prepared (a) Cu_2S NBs, (b) ZnIn_2S_4 NSs, (c) $\text{Cu}_2\text{S}/\text{ZnIn}_2\text{S}_4$, (d) $\text{Cu}_2\text{S}/\text{ZnIn}_2\text{S}_4\text{-mix}$. The insets are corresponding pore diameter distribution diagrams.

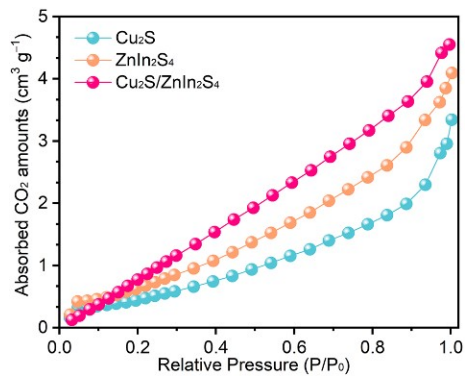


Fig. S22. CO₂ adsorption isotherms of the as-prepared Cu₂S NBs, ZnIn₂S₄ NSs, Cu₂S/ZnIn₂S₄ HHNCs.

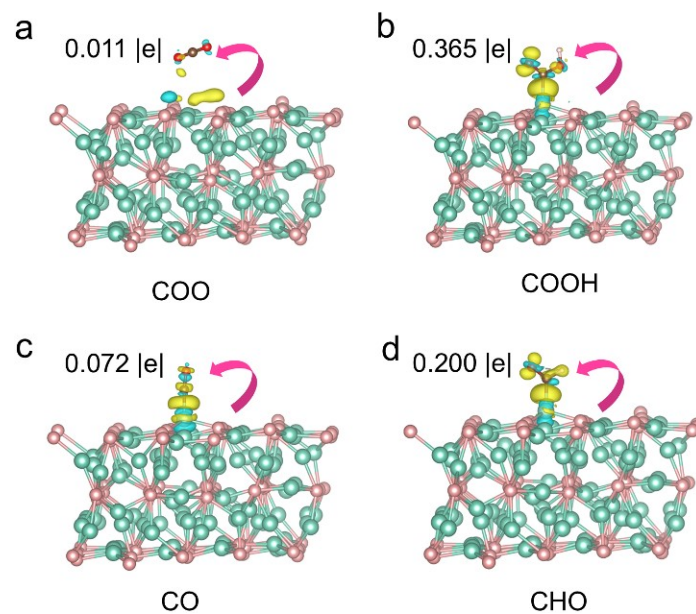


Fig. S23. Charge density difference maps for CO_2 intermediate adsorption on the Cu_2S . The cyan and the yellow region agminated at the heterogeneous interface represent charge depletion and charge accumulation, respectively.

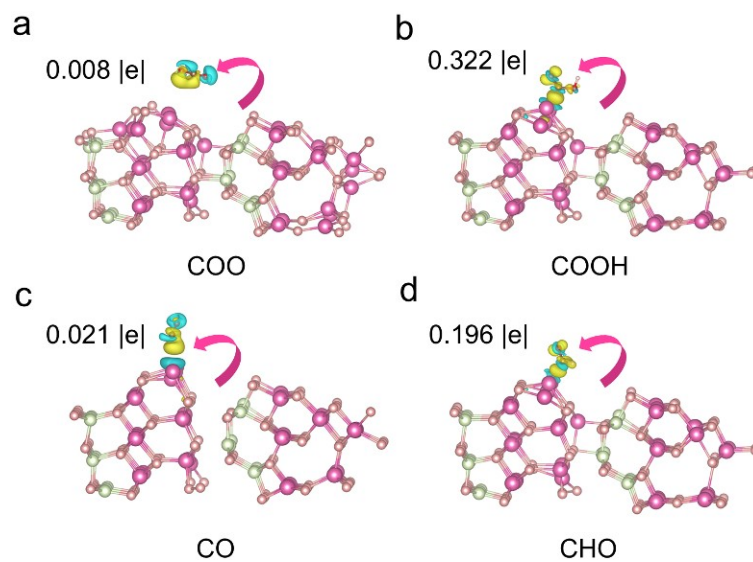


Fig. S24. Charge density difference maps for $^*\text{CO}_2$ intermediate adsorption on the ZnIn_2S_4 . The cyan and the yellow region agminated at the heterogeneous interface represent charge depletion and charge accumulation, respectively.

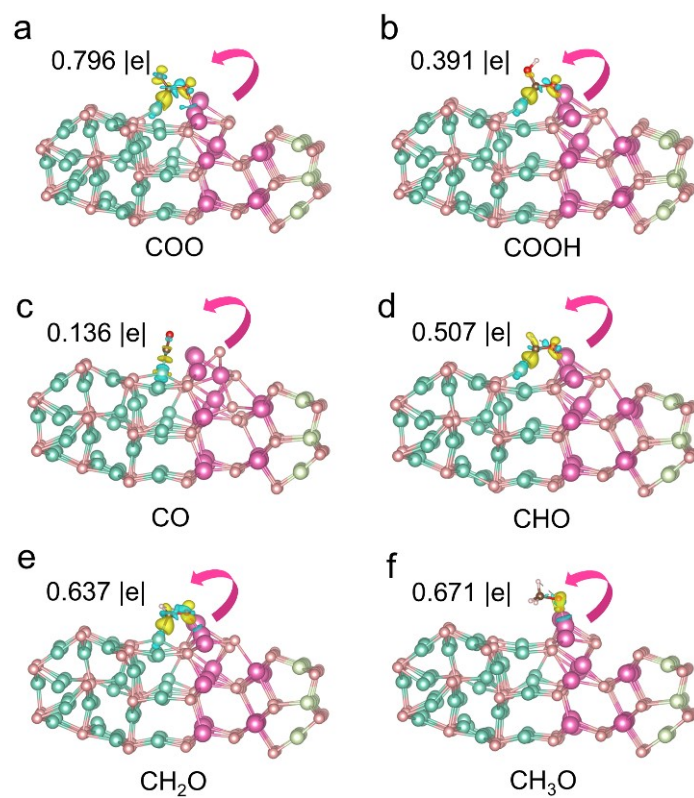


Fig. S25. Charge density difference maps for CO_2 intermediate adsorption on the $\text{Cu}_2\text{S}/\text{ZnIn}_2\text{S}_4$. The cyan and the yellow region agminated at the heterogeneous interface represent charge depletion and charge accumulation, respectively.

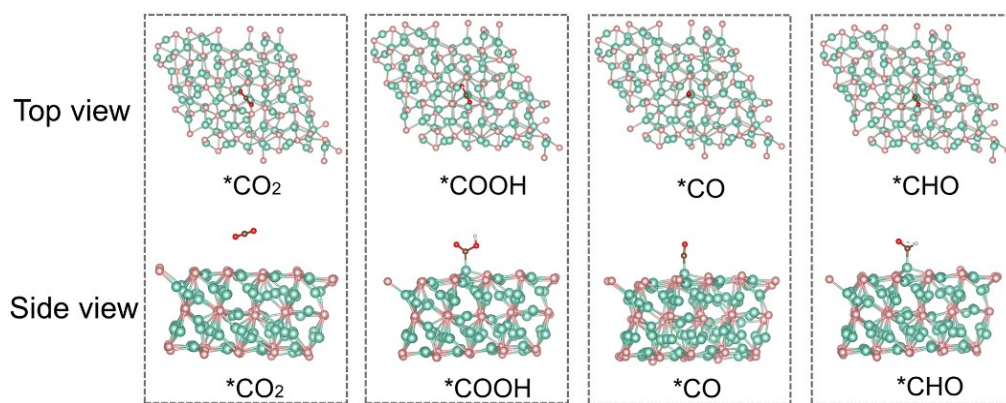


Fig. S26. Top and side view of the optimized ball-stick mode of CO₂ intermediate on Cu₂S.

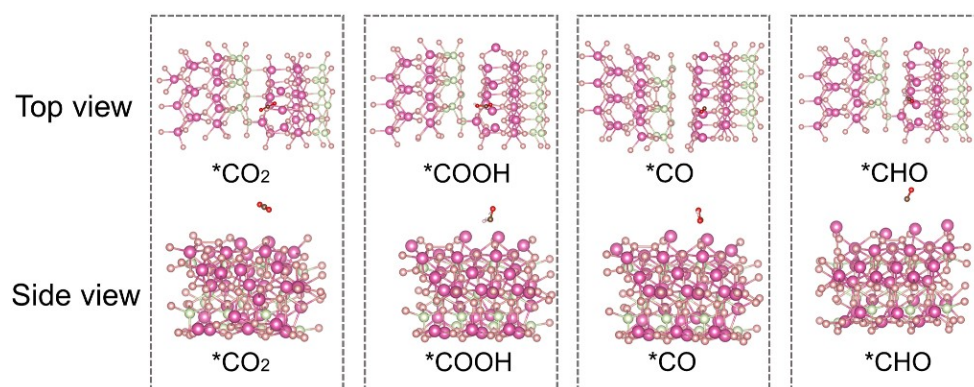


Fig. S27. Top view and side view of the optimized ball-stick mode of CO₂ intermediate on ZnIn₂S₄.

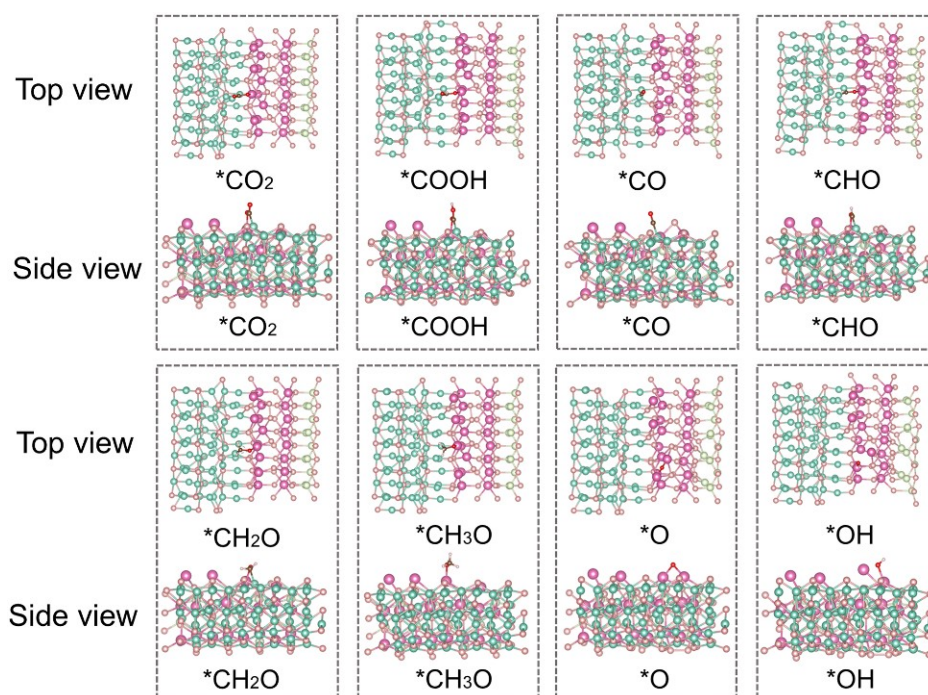


Fig. S28. Top view and side view of the optimized ball-stick mode of CO₂ intermediate on Cu₂S/ZnIn₂S₄.

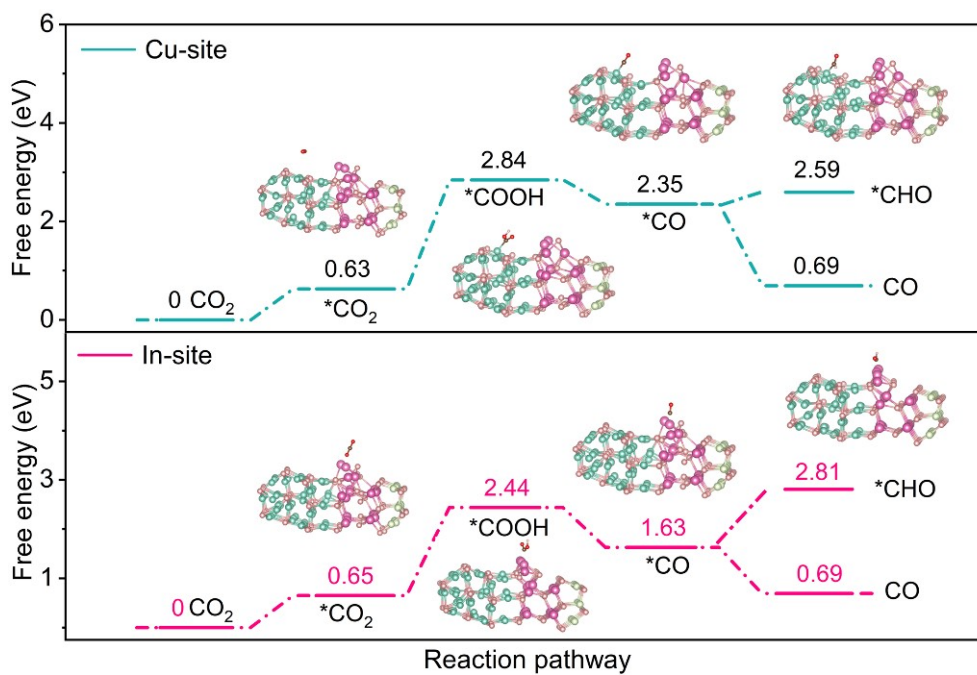


Fig. S29. Reaction pathways for CO₂ photocatalysis on Cu site and In site of Cu₂S/ZnIn₂S₄ HHNCs and calculated Gibbs free energies of reaction intermediates.

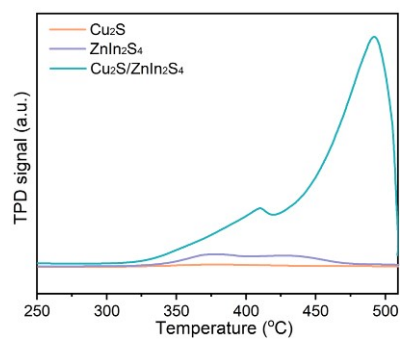


Fig. S30. CO-TPD profiles of the Cu₂S NBs, ZnIn₂S₄ NSs and Cu₂S/ZnIn₂S₄ HHNCs.

3. Supplementary Tables:

Table S1 Photocatalytic CO₂ reduction performance of as-prepared photocatalysts under various conditions.

Photocatalyst	Reaction medium	Light source	Product	Yield	CH ₄
				($\mu\text{mol g}^{-1} \text{h}^{-1}$)	Selectivity
Cu₂S	Water vapor	300 W Xe lamp ($\lambda > 400 \text{ nm}$)	CO	1.47	53%
			CH ₄	1.67	
ZnIn₂S₄	Water vapor	300 W Xe lamp ($\lambda > 400 \text{ nm}$)	CO	4.19	35%
			CH ₄	2.3	
Cu₂S/ZnIn₂S₄-1	Water vapor	300 W Xe lamp ($\lambda > 400 \text{ nm}$)	CO	1.5	91%
			CH ₄	16.7	
Cu₂S/ZnIn₂S₄-2 (Cu₂S/ZnIn₂S₄)	Water vapor	300 W Xe lamp ($\lambda > 400 \text{ nm}$)	CO	1.7	93%
			CH ₄	22.7	
Cu₂S/ZnIn₂S₄-3	Water vapor	300 W Xe lamp ($\lambda > 400 \text{ nm}$)	CO	1.0	88%
			CH ₄	7.7	
Cu₂S/ZnIn₂S₄- mix	Water vapor	300 W Xe lamp ($\lambda > 400 \text{ nm}$)	CO	2.5	60%
			CH ₄	3.7	
Without catalyst	Water vapor	300 W Xe lamp ($\lambda > 400 \text{ nm}$)	CO	n.d.	--
			CH ₄	n.d.	
Cu₂S/ZnIn₂S₄-2 (Cu₂S/ZnIn₂S₄)	--	300 W Xe lamp ($\lambda > 400 \text{ nm}$)	CO	n.d.	--
			CH ₄	n.d.	
Cu₂S/ZnIn₂S₄-2 (Cu₂S/ZnIn₂S₄) with saturated Ar	Water vapor	300 W Xe lamp ($\lambda > 400 \text{ nm}$)	CO	n.d.	--
			CH ₄	n.d.	
Cu₂S/ZnIn₂S₄-2 (Cu₂S/ZnIn₂S₄)	Water vapor	--	CO	n.d.	--
			CH ₄	n.d.	

Table S2 Comparison of CO₂ photoreduction performance by Cu₂S/ZnIn₂S₄ HHNCs and previously reported Cu-based, Zn-based and In-based catalysts.

Photocatalyst	Light source	Product	Yield ($\mu\text{mol g}^{-1} \text{h}^{-1}$)	CH ₄ Selectivity	Reference
Cu ₂ S/ZnIn ₂ S ₄	300 W Xe lamp ($\lambda > 400 \text{ nm}$)	CO	1.7	93%	This work
		CH ₄	22.7		
CuInSnS ₄	300 W Xe lamp ($\lambda > 420 \text{ nm}$)	CO	2.4	67%	10
		CH ₄	5.8		
In ₄ SnS ₈	300 W Xe lamp ($\lambda > 420 \text{ nm}$)	CO	20.9	57%	11
		CH ₄	23.9		
CuS-Bi ₂ WO ₆	300 W Xe lamp	CO	33.9	33%	12
		CH ₄	16.4		
Ga ₂ S ₃ /CuS	300 W Xe lamp	CO	2.2	89%	13
		CH ₄	18.8		
Vs-CuIn ₅ S ₈	300 W Xe lamp ($\lambda > 420 \text{ nm}$)	CO	0	100%	14
		CH ₄	8.7		
Cu ₄ (SO ₄)(OH) ₆	300 W Xe lamp ($\lambda > 800 \text{ nm}$)	CO	21.9	16%	15
		CH ₄	4.1		
In ₂ S ₃ /In ₂ O ₃	300 W Xe lamp ($\lambda > 420 \text{ nm}$)	CO	2.8	95%	16
		CH ₄	16.5		
CuInP ₂ S ₆	Solar simulator	CO	3.4	66%	17
		CH ₄	6.6		
Cu ₂ ZnSnS ₄ /Pt/g-C ₃ N ₄	400 W Xe lamp ($\lambda > 420 \text{ nm}$)	CO	17.4	31%	18
		CH ₄	8.0		
WO ₃ /Au/In ₂ S ₃	300 W Xe lamp ($\lambda > 420 \text{ nm}$)	CO	0	100%	19
		CH ₄	0.4		
Co ₃ O ₄ /ZnIn ₂ S ₄	300 W Xe lamp ($\lambda > 420 \text{ nm}$)	CO	11.1	53%	20
		CH ₄	12.8		

Ag-Pt/ZnO-ZIF-8	300 W Xe lamp ($\lambda = 320-780$ nm)	CO	0.2	98%	21
		CH ₄	16.2		
Vo-Zn-CoO	300 W Xe lamp	CO	9.7	64%	22
		CH ₄	17.7		

Supplementary References:

- 1 S. Sun, M. Watanabe, J. Wu, Q. An, T. Ishihara, *J. Am. Chem. Soc.*, 2018, **140**, 6474-6482.
- 2 G. Kresse, D. Joubert, *Phys. Rev. B*, 1999, **59**, 1758-1775.
- 3 G. Kresse, J. Hafner, *Phys. Rev. B*, 1993, **47**, 558-561.
- 4 G. Kresse, J. Furthmüller, *Phys. Rev. B*, 1996, **54**, 11169-11186.
- 5 J.P. Perdew, K. Burke, M. Ernzerhof, *Phys. Rev. Lett.*, 1996, **77**, 3865-3868.
- 6 H.J. Monkhorst, J.D. Pack, *Phys. Rev. B*, 1976, **13**, 5188-5192.
- 7 K. Momma, F.J.J.o.A.C. Izumi, 2011, **44**, 1272-1276.
- 8 J.K. Nørskov, J. Rossmeisl, A. Logadottir, L. Lindqvist, J.R. Kitchin, T. Bligaard, H. Jónsson, *J. Phys. Chem. B*, 2004, **108**, 17886-17892.
- 9 Johnson, R., <http://cccbdb.nist.gov/>.
- 10 Y. Chai, Y. Kong, M. Lin, W. Lin, J. Shen, J. Long, R. Yuan, W. Dai, X. Wang, Z. Zhang, *Nat. Commun.*, 2023, **14**, 6168.
- 11 Y. Chai, Y. Chen, J. Shen, M. Ni, B. Wang, D. Li, Z. Zhang, X. Wang, *ACS Catal.*, 2021, **11**, 11029-11039.
- 12 J. Tian, Y. Zhang, Z. Shi, Z. Liu, Z. Zhao, J. Li, N. Li, H. Huang, *Angew. Chem. Int. Ed.*, 2024, **64**, e202418496.
- 13 Y. Sun, K. Lai, N. Li, Y. Gao, L. Ge, *Appl. Catal. B: Environ. Energy*, 2024, **357**, 124302.
- 14 X. Li, Y. Sun, J. Xu, Y. Shao, J. Wu, X. Xu, Y. Pan, H. Ju, J. Zhu, Y. Xie, *Nat. Energy*, 2019, **4**, 690-699.
- 15 X. Li, L. Li, G. Chen, X. Chu, X. Liu, C. Naisa, D. Pohl, M. Löffler, X. Feng, *Nat. Commun.*, 2023, **14**, 4034.
- 16 K. Lai, Y. Sun, N. Li, Y. Gao, H. Li, L. Ge, T. Ma, *Adv. Funct. Mater.*, 2024, 2409031.
- 17 C.-H. Chiang, C.-C. Lin, Y.-C. Lin, C.-Y. Huang, C.-H. Lin, Y.-J. Chen, T.-R. Ko, H.-L. Wu, W.-Y. Tzeng, S.-Z. Ho, Y.-C. Chen, C.-H. Ho, C.-J. Yang, Z.-W. Cyue, C.-L. Dong, C.-W. Luo, C.-C. Chen, C.-W. Chen, *J. Am. Chem. Soc.*, 2024, **146**, 23278-23288.

- 18 A. Raza, H. Shen, A.A. Haidry, *Appl. Catal. B: Environ.*, 2020, **277**, 119239.
- 19 H. Li, Y. Gao, Y. Zhou, F. Fan, Q. Han, Q. Xu, X. Wang, M. Xiao, C. Li, Z. Zou, *Nano Letters*, 2016, **16**, 5547-5552.
- 20 C. Cheng, H. Xu, M. Ni, C. Guo, Y. Zhao, Y. Hu, *Appl. Catal. B: Environ. Energy*, 2024, **345**, 123705.
- 21 Q. Li, Q. Wang, Y. Zeng, Y. Xu, X.-K. Gu, M. Ding, *Adv. Funct. Mater.*, 2024, **35**, 2416975.
- 22 K. Chen, T. Jiang, T. Liu, J. Yu, S. Zhou, A. Ali, S. Wang, Y. Liu, L. Zhu, X. Xu, *Adv. Funct. Mater.*, 2022, **32**, 2109336.